Band structure, *g*-factor, and spin relaxation in *n*-type InAsP alloys

Sunil K. Thapa,[1,*] Rathsara R. H. H. Mudiyanselage,[2,*] Thalya Paleologu,[1] Sukgeun Choi,[3] Zhuo Yang,[4] Y. Kohama,[4] Y. H. Matsuda,[4] Joseph Spencer,[2] Brenden A. Magill,[2] Chris J. Palmstrøm,[3] Christopher J. Stanton,[1,†] and Giti A. Khodaparast[2,‡]

[1]*Department of Physics, University of Florida, Gainesville, Florida 32611, USA*
[2]*Department of Physics, Virginia Tech, Blacksburg, Virginia 24061, USA*
[3]*Department of Electrical and Computer Engineering, University of California, Santa Barbara, California 93106, USA*
[4]*Institute for Solid State Physics, University of Tokyo, Kashiwanoha, Kashiwa, Chiba 277-8581, Japan*

(Received 27 March 2023; accepted 23 August 2023; published 14 September 2023)

We present experimental and theoretical studies of the magneto-optical properties of *n*-type $InAs_xP_{1-x}$ films in ultrahigh magnetic fields at room temperature. We compare Landau level and band structure calculations with observed cyclotron resonance (CR) measurements and extract effective *g*-factors and CR masses for two different alloy concentrations, $x = 0.07$ and $x = 0.34$. In addition, we employ time-resolved magneto-optical Kerr measurements on these ternary alloys to explore the spin relaxation time. These alloys have immense prospects for quantum communication devices and *g*-factor engineering, and our study provides insights into this underexplored narrow-gap system.

DOI: 10.1103/PhysRevB.108.115202

I. INTRODUCTION

Historically, InAsP alloys have been important for device applications due to the possibility of band gap engineering, which can vary from around 0.36 to 1.35 eV (∼3.4 μm to 900 nm), covering parts of the midinfrared to the near infrared. Examples of device applications include broadband photodetectors [1], mid-IR lasers [2], and optical telecommunications [3]. Another important materials system in this family is InGaAsP, which can be lattice matched to InP. InGaAsP systems have been widely used for optoelectronic components, such as laser diodes, detectors, waveguides, and modulators [4].

When it comes to photodetectors for quantum information and sensing, to preserve the entanglement, as suggested by Vrijen and Yablonovitch [5], it is important to fabricate photodetectors using a material that has a conduction band effective *g*-factor much smaller than the valence band, so that the photodetector can excite equally to the spin split states. The tunability of the electron effective *g*-factor (including $g = 0$) can provide a major advancement for semiconductor-based quantum communication applications. Here we demonstrate, through an experimental and theoretical study, that the InAsP system is indeed a very good candidate in this regard [5], and the correct choice of alloying can lead to a system with an almost zero value for the effective *g*-factor. Detailed band structure calculations and analysis of InAsP alloys have rarely been done [6–8].

In this paper, we focus on less explored characteristics of the *n*-type ternary alloy of indium arsenide phosphide ($InAs_xP_{1-x}$) grown on an InP substrate. These characteristics include their band structure, cyclotron resonance (CR) masses, *g*-factor tunability, and spin dynamics. We performed experimental high magnetic field CR experiments as well as time-resolved Kerr rotation measurements and compared our results to theoretical calculations.

Our 1.2 μm thick $InAs_{0.07}P_{0.93}$ and $InAs_{0.34}P_{0.66}$ samples were grown on semi-insulating InP(001) wafers; they were made *n* type with Si doping, with electron densities of 9.3×10^{16} and 1.5×10^{17} cm^{-3} for $x = 0.07$ and 0.34, respectively. The alloy compositions were determined by high-resolution x-ray diffraction, and the carrier concentrations were measured by an electrochemical capacitance-voltage profiler.

The results presented in this study go beyond InAs [9–12] and InP [13–15], which are two widely researched III-V compound semiconductors when it comes to their band structures, *g*-factor engineering, and spin dynamics. We should note that, when it comes to the dynamical aspects of InAsP, previous studies included only the spin relaxation dynamics in undoped InAsP films, employing spin-polarized differential transmission and dynamics of localized excitonic transitions [16,17]. In this study, beyond CR measurements, we employed ultrafast time-resolved Kerr rotation (TRKR) measurements on *n*-type $InAs_xP_{1-x}$ ternary alloys to probe spin relaxation dynamics, which provided an additional window to detect the effective *g*-factor.

In our work, both measurements were performed at *room temperature* (RT) because the extracted information could be important for developing practical devices. Measuring CR at RT is somewhat difficult owing to the low mobilities of the carriers. As a result, the measurements must be performed at very high magnetic fields, on the order of 100 T. This complicates the calculations since in narrow-gap semiconductors (NGSs), the nonparabolicity of the conduction band E vs the k

*These authors contributed equally to this work.
†Corresponding author: stanton@phys.ufl.edu
‡Corresponding author: khoda@vt.edu

 ©2023 American Physical Society

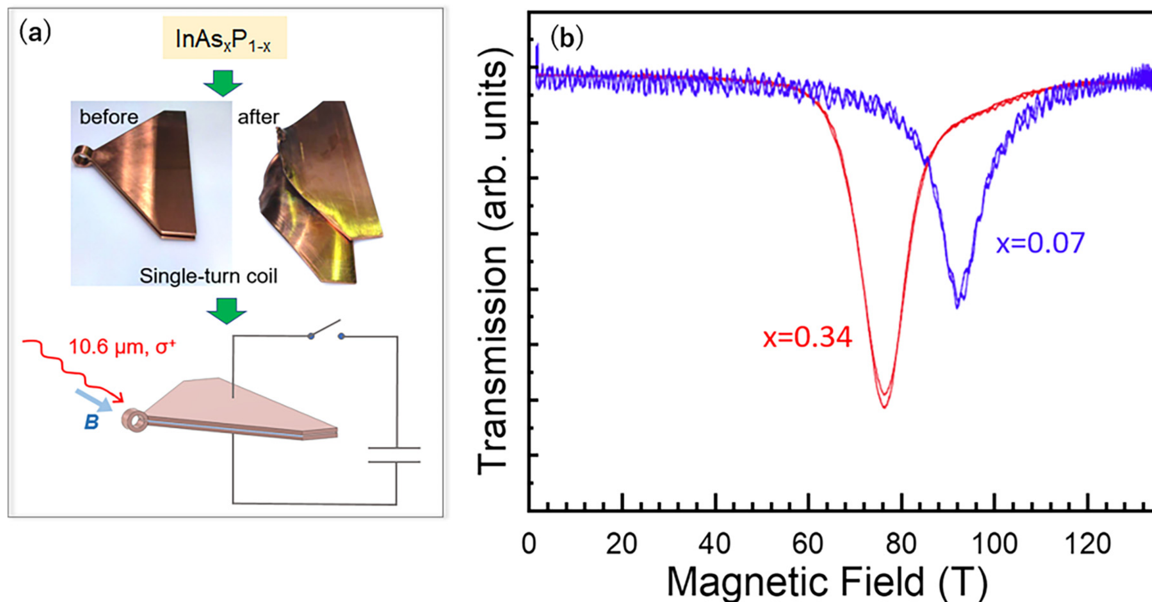

FIG. 1. Experimental measurements of CR in $InAs_xP_{1-x}$ alloys at $T = 300$ K. (a) Experimental setup. (b) Detected transmission change for $x = 0.07$ (blue) and $x = 0.34$ (red), sweeping the field up and down, in which the traces overlap, demonstrating reproducible observations. The fits to the CR traces confirm the carrier density, which is on the order of 1.0×10^{17} cm^{-3}.

dispersion relation means that the Landau levels are no longer linear in the applied magnetic field. As a result, the CR masses will differ from the conduction band edge effective mass and will depend on the magnetic field.

II. EXPERIMENTAL CYCLOTRON RESONANCE IN ULTRAHIGH MAGNETIC FIELDS

Our CR measurements were conducted in the infrared regime by employing pulsed ultrahigh magnetic fields (<150 T) generated using a single-turn coil technique [18–20]. The external field was applied along the growth direction. The source of infrared radiation was a CO_2 laser. The transmission data were obtained by means of a fast liquid-nitrogen-cooled HgCdTe detector, where a multichannel digitizer placed in a shielded room recorded the signals from the detector as well as the pickup coil. The measurements were carried out in the Megagauss laboratory at the University of Tokyo. In Fig. 1(a), we show the CR measurement process for $InAs_xP_{1-x}$ at RT with σ^+ excitation (electron active) energy of 117 meV (10.6 μm), and Fig. 1(b) shows the transmission coefficients for $x = 0.07$ (blue) and $x = 0.34$ (red). The estimated cyclotron masses $M_{\rm CR}$ using the resonant magnetic field B_r are $0.0907m_0$ and $0.0751m_0$, respectively, where m_0 is the free electron mass. Also, using the linewidth of the resonances, the mobilities are estimated to be 994 cm^2 V^{-1} s^{-1} for $x = 0.07$ and 813 cm^2 V^{-1} s^{-1} for $x = 0.34$.

III. CALCULATIONS OF THE CONDUCTION BAND LANDAU LEVELS, CYCLOTRON EFFECTIVE MASS, AND THE EFFECTIVE g-FACTOR

To understand magneto-optical responses in NGSs such as InAs, one typically utilizes a modified or extended Pidgeon-Brown-type model [21] which is based on an eight-band $\mathbf{k}\cdot\mathbf{P}$ model that includes the twofold spin degenerate conduction, heavy hole, light hole, and spin-orbit split bands and allows for coupling to higher-order bands. This model works extremely well for bulk materials as well as for heterostructures such as multiple quantum wells for binary materials. While, in principle, the Pidgeon-Brown model can be applied to alloys and tertiary materials such as InAsP, the difficulty lies in determining how to interpolate the many parameters that go into the Pidgeon-Brown model [21] such as the band gaps E_g; optical matrix element P; Luttinger parameters γ_1, γ_2, and γ_3; and the F parameter (which takes into account the coupling to higher-order bands) between the binary materials (i.e., InAs and InP for the InAsP alloy system).

Focusing solely on the conduction band CR, one can use an easier model based on a simplified Kane model. We previously applied this model with success to model effective masses in near-surface InAs quantum wells [12]. Here we extend this model to include ternary alloy materials. In the simplest model for a NGS, the dispersion for the conduction band in zero magnetic fields is given by:

$$\epsilon(1+\alpha\epsilon) = \frac{\hbar^2k^2}{2m_0^*}. \quad (1)$$

In this expression, the dispersion relation is quadratic in k for small energies and becomes linear in k for large energies. The nonparabolicity parameter α is given by the inverse band gap energy $\alpha = 1/E_g$, ϵ is the conduction band energy with respect to the bottom of the conduction band, k is the wave vector, and m_0^* is the conduction band effective mass at the band edge ($k = 0$). This model works very well for the conduction band of NGSs such as InAs and InSb and is clearly extended to medium-gap (and large-gap) materials like InP since α is even smaller.

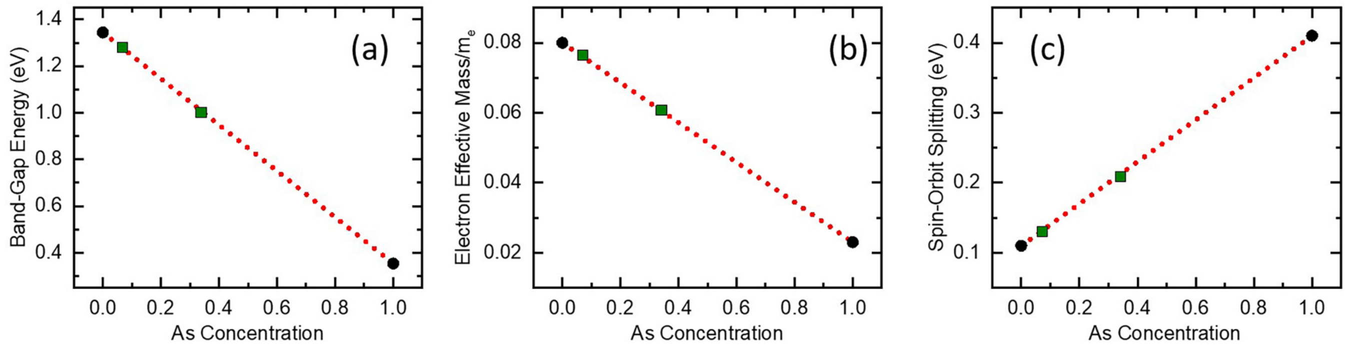

FIG. 2. The band gap, effective mass, and spin-orbit splitting Δ for $InAs_xP_{1-x}$ as a function of x, using linear interpolations between room temperature values for InP ($x = 0$) and InAs ($x = 1$), m_e is the free electron mass.

When a magnetic field $\mathbf{B} = B\hat{\mathbf{z}}$ is applied, one can make the replacement [22–24]:

$$k^2 = k_x^2 + k_y^2 + k_z^2 \rightarrow k_z^2 + \frac{2m_0^*}{\hbar^2}\left(n + \frac{1}{2}\right)\hbar\omega_{c0}, \quad (2)$$

where $\omega_{c0} = \frac{eB}{m_0^*}$ is the band edge CR frequency and $n = 0, 1, 2, \ldots$ is the Landau level index. Therefore, after adding a Zeeman term, we can rewrite Eq. (1) as:

$$\epsilon(1 + \alpha\epsilon) = \frac{\hbar^2 k_z^2}{2m_0^*} + \left(n + \frac{1}{2}\right)\hbar\omega_{c0} \pm \frac{1}{2}\mu_B g_0^* B, \quad (3)$$

where g_0^* is the *band edge* effective g-factor and μ_B is the Bohr magneton. To calculate g_0^* we use Eq. (A5) from Yuan *et al.* [12]:

$$g_0^* = 2\left[1 + \left(1 - \frac{1}{m_0^*}\right)\frac{\Delta}{3\epsilon_g + 2\Delta}\right], \quad (4)$$

where ϵ_g is the band gap energy and Δ is the valence band spin-orbit splitting. This approximation works well for NGSs but, as we see later, needs to be slightly modified for medium-gap materials. In our simple model for the conduction band of $InAs_xP_{1-x}$, we follow Zhao *et al.* [25] and take a linear interpolation of the band gap $\epsilon_g(x)$ as well as $m_0^*(x)$ and $\Delta(x)$. We should note that we did not take into account any bowing. We note that the linear interpolation of the band edge effective mass agrees with the experimental results at 77 K from Nicholas *et al.* (we refer to their Fig. 2 in [6]). In Figs. 2(a)–2(c) we present the band gap, the electron effective mass, and the spin-orbit splitting at RT as a function of the alloy concentration x ($x = 1$ for InAs and $x = 0$ for InP).

Taking Eq. (3), setting $k_z = 0$, and solving for the conduction energy band, we get an expression for the Landau levels (for $k_z = 0$) as a function of the level index n and magnetic field B:

$$\epsilon_{c,n} = \frac{-1 + \sqrt{1 + 4\alpha[(n + \frac{1}{2})\hbar\omega_{c0} \pm \frac{1}{2}\mu_B g_0^* B]}}{2\alpha}. \quad (5)$$

Here the plus sign corresponds to spin up (↑), and the minus sign corresponds to spin down (↓).

In Fig. 3 we plot the calculated conduction band Landau level fan diagrams (for $k_z = 0$), using Eq. (5) and the linear interpolations shown in Fig. 2 as a function of B for $InAs_xP_{1-x}$ for $x = 0$, 0.07, 0.34, and 1.0. We see that at high magnetic fields and large Landau level indices, the Landau levels are no longer linear in B. The curvature of the Landau levels with increasing B increases as x is varied from 0 to 1. This can be attributed to the decreasing band gap with increasing x, which results in the bands becoming more nonparabolic, which in turn leads to deviations from the linear in B dependence to that of $\sqrt{B}$. This occurs even for $x = 0$ and $x = 0.07$.

In Fig. 3, we also show with green arrows where the simple theory predicts a CR transition to occur for our laser excitation at 0.117 eV (10.6 μm). For $x = 0.07$ and $x = 0.34$, we expect to see CR at $B = 92.3$ T and $B = 77.4$ T, respectively. This agrees well with the observed resonances at $B = 91.7$ T and $B = 75.9$ T [see Fig. 1(b)]. In addition, for $x = 0.34$, we plot a yellow arrow that corresponds to a weaker $n = 1$ to $n = 2$ transition. Our theory predicts that this transition should occur at $B = 96.4$ T and should give rise to a small shoulder in the CR line shape. This agrees very well with the observed small shoulder in the experimental $x = 0.34$ curve (see Fig. 1) as well as with Fig. 4, where we compare the theoretical calculations with the experimental data.

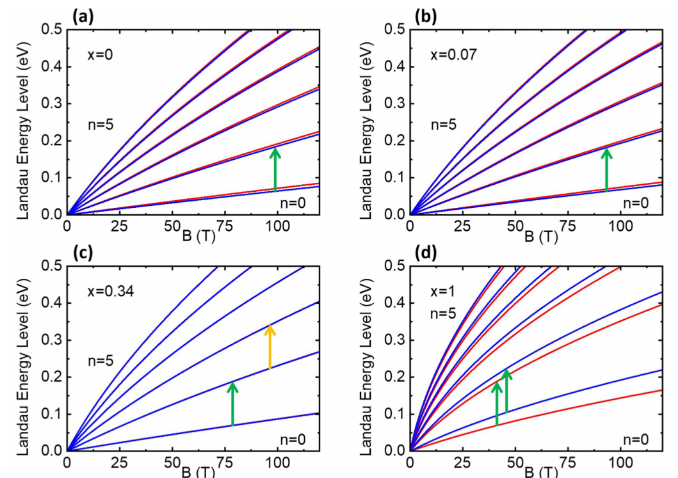

FIG. 3. Calculated Landau levels from our simple model in $InAs_xP_{1-x}$ for (a) $x = 0.0$, (b) $x = 0.07$, (c) $x = 0.34$, and (d) $x = 1.0$. All energy values are with respect to the bottom of the conduction band. Green arrows show the dominant transition for excitation by a 10.6 μm laser. The yellow arrow for $x = 0.34$ shows a secondary transition from the $n = 1$ Landau level to the $n = 2$ Landau level and gives rise to the small shoulder feature seen in Fig. 4 as well as in Fig. 1(b).

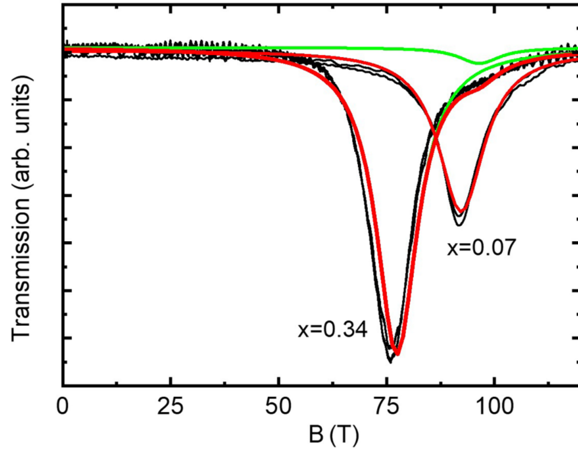

FIG. 4. Comparison of the experimental CR (solid black curves) with the calculated CR (green and red curves). The bright green curves show the two different predicted transitions for $x = 0.34$. The first transition is mostly hidden behind the red $x = 0.34$ curve, which represents the sum of the two predicted transitions. The red curves show the predicted CR results for $x = 0.34$ (left) and $x = 0.07$ (right).

We now compare the cyclotron masses between the experiment and our calculations. The cyclotron mass for the $n = 0 \rightarrow 1$ transition can be obtained from the conservation of energy at the resonance. It is defined in terms of the bare electronic mass m_e as [18]:

$$M_{\mathrm{CR}} = \frac{2\mu_B B}{\epsilon_{c1,\uparrow} - \epsilon_{c0,\uparrow}} m_e. \tag{6}$$

Figure 5 shows the magnetic field dependence of the cyclotron mass calculated using Eq. (6). Clearly, with increasing As concentration x, there is an increase in nonlinearity which is reflective of the increased coupling between the conduction and valence bands. Near $B = 0$ T, the cyclotron mass M_{CR} is equal to the bare electronic effective masses. For InP ($x = 0.0$) and InAs ($x = 1.0$), the cyclotron mass near $B = 0$ T is equal to the conduction band effective mass m_0^* used in our $\mathbf{k} \cdot \mathbf{P}$ calculations. At $\mathbf{B} = \mathbf{B}_r$ (where B_r is the resonance field), our calculated CR mass from the simple model shows excellent agreement with the experimental observation, as shown in Table I. In addition, the carrier mobility can also be estimated from the FWHM of the CR. We note that, due to the measurements at very high magnetic field, the effective mass is not equal to the bare effective mass and the mobility is not equal to the dc mobility.

TABLE I. Comparison of calculated and measured effective masses in ultrahigh magnetic fields.

	M_{CR}	
As concentration x	Theory	(Expt.)
0.07	0.0913	0.0907
0.34	0.0766	0.0751

To find the dependence of g^* on the magnetic field as well as on the As concentration for the lowest Landau Level, $n = 0$, we define it as follows:

$$g^* = \frac{\epsilon_{c0,\uparrow} - \epsilon_{c0,\downarrow}}{\mu_B B}, \quad B \neq 0, \tag{7}$$

where $\epsilon_{c0,\uparrow}$ and $\epsilon_{c0,\downarrow}$ refer to the calculated conduction bands (for $n = 0$) with up and down spins, respectively [see Eq. (5)]. Figure 6 shows the calculated g-factors using Eq. (4) for the four different As concentrations: $x = 0.0$ (purple), 0.07 (blue), 0.34 (orange), and 1.00 (green). We observe that for all B, the effective g-factor decreases from a small positive number to a large negative number as x increases from 0 to 1, where $g^* \approx 0$ at $x = 0.34$. This suggests the existence of a well-defined As concentration in InAsP such that $g^* \approx 0$ at $B = 0$.

The g-factor for InP ($x = 0.0$) starts as a small positive number, which at $B = 0$ is mostly determined by its fundamental parameters such as the band gap, spin splitting, and Kane energy E_p [18], which remains almost unaltered by the magnetic field B. When x is increased to 0.07, the magnitude decreases but still remains positive throughout. It is when x increases to 0.34 that we observe a significant change. The

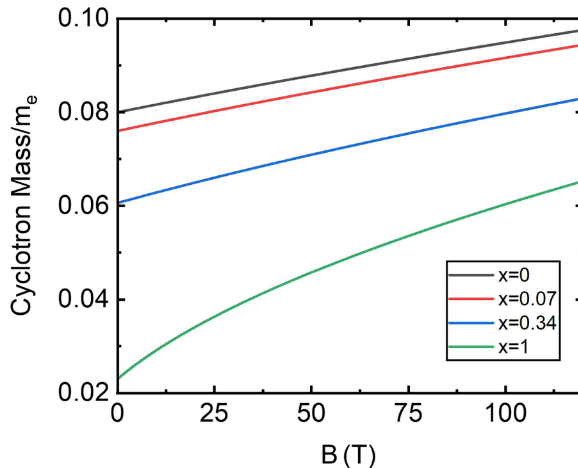

FIG. 5. Calculated CR mass for $InAs_xP_{1-x}$ for different As concentrations. m_e is the free electron mass.

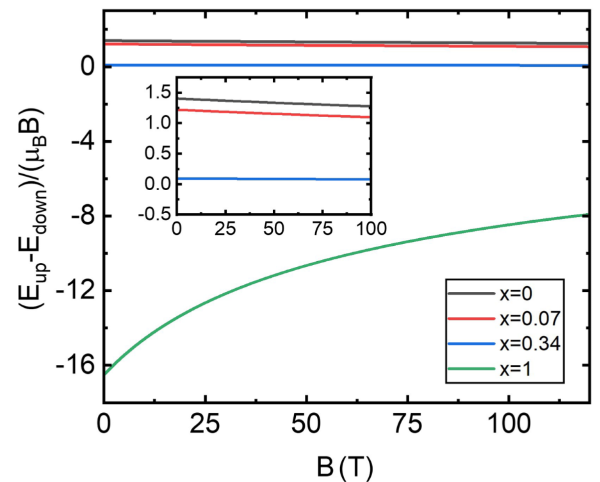

FIG. 6. Magnetic field dependence of g^* as a function of magnetic field, plotted for $InAs_xP_{1-x}$ with different values of x.

g-factor becomes very close to zero at $B \approx 0$ and stays well below 0.5 over all the magnetic field ranges.

For $x = 1$, the semiconductor is pure InAs. The band edge g-factor has a large magnitude, and it is negative. This can be seen from Eq. (4) and this fact occurs because InAs has a much smaller band gap than InP. The g-factor changes rapidly to a smaller magnitude (but remains negative) as the magnetic field is increased. All these facts point to the viability of a zero-g-factor InAsP alloy at $B = 0$, with a well-defined As concentration [26].

IV. ULTRAFAST TIME-RESOLVED KERR ROTATION

Our Kerr rotation measurements at RT were performed on $InAs_{0.34}P_{0.66}$ using a degenerate time-resolved pump-probe technique. The pump energy was 1.305 eV (950 nm), with σ^- polarization and 120 mW of power (corresponding to a fluence of $\sim$7 $\mu J/cm^2$), where we used a Ti:sapphire oscillator with a 100 fs pulse width and 80 MHz repetition rate. The estimated excited carrier density was $\sim 3\times10^{17}$ cm^{-3}. Although the same excitation energy was used for the probe pulses, the polarization was linear, and the intensity was about 100 times lower than the pump pulses. Figure 7(a) shows the TRKR profile on a short timescale of 300 ps.

A biexponential fit results in two time constants, $\tau_1 = 7.24 \pm 1.15$ ps and $\tau_2 = 38.2 \pm 1.66$ ps. Figure 7(b) is a similar data set at the same pump energy and intensity, with the measurements recorded for a longer time range of 1300 ps but with a larger time step. This data set is selectively fitted with exponential decay functions. The fit between 13.0 and 306 ps (in orange) results in a shorter time constant τ_3 of 39.1 ± 1.38 ps, and the fit between 173 and 1213 ps (in magenta) gives a much longer time constant τ_4 of 394 ± 39.6 ps. In the upcoming sections, we relate these time constants to various spin relaxation processes.

Unfortunately, to precisely theoretically model the ultrafast Kerr rotation, we need both the conduction band and valence band contributions. As a result, we cannot utilize the simple model used to determine the conduction band CR. Instead, theoretical explorations of $InAs_xP_{1-x}$ start with the single-particle electronic band structure calculation, using the eight-band Pidgeon-Brown model for a bulk semiconductor in an external magnetic field of $\mathbf{B} = \mathbf{B_z}\hat{z}$ [18,27]. The effective mass Hamiltonian of the system is given by:

$$H = H_L + H_Z, \tag{8}$$

where H_L is the $\mathbf{k}$-dependent Landau Hamiltonian and H_Z is the $\mathbf{k}$-independent Zeeman Hamiltonian. The explicit matrix representation is adopted from elsewhere [18], wherein the matrix elements are expressed in terms of empirical parameters such as the band gap E_g, the spin-orbit splitting Δ, the Luttinger parameters (γ_1, γ_2, and γ_3), the conduction electron effective mass m_c, and the Kane energy E_p. For $InAs_xP_{1-x}$, these parameters are all estimated by using linear interpolation between InAs and InP with bowing parameters wherever applicable [28] and were determined to produce agreement with the experimental CR data. Using envelope functions within the axial approximation, the energy eigenvalues and eigenfunctions were calculated.

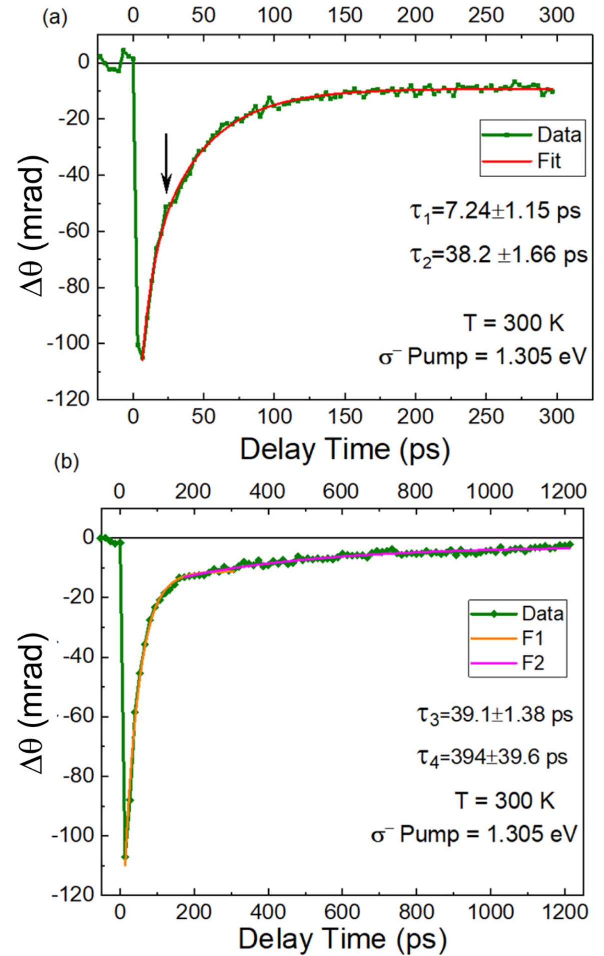

FIG. 7. (a) TRKR profile for a short duration of 300 ps in $InAs_{0.34}P_{0.66}$. The green curve is the experimental plot, and the red curve is the biexponential fit with the time constants $\tau_1 = 7.24 \pm 1.15$ ps and $\tau_2 = 38.2 \pm 1.66$ ps. The vertical arrow points to the biexponential nature of the data. (b) TRKR profile for a longer duration of 1300 ps with τ_3 of 39.1 ± 1.38 ps from fit F1 (in orange) and τ_4 of 394 ± 39.6 ps from fit F2 (in magenta).

In nonmagnetic semiconductors such as n-type GaAs [29] and n-type $InAs_xP_{1-x}$, the spin polarization of conduction electrons can be achieved by ultrafast photoexcitation with circularly polarized light even in the absence of the magnetic field. For example, Fig. 8 shows a sample schematic band structure of $InAs_xP_{1-x}$ and the allowed optical transitions. For circularly polarized light, the green vertical line shows the heavy hole (HH) transition, the brown line shows the light hole (LH) transition, and the black line shows the split-off hole (SH) transition to the conduction band for $\alpha\uparrow$ and $\alpha\downarrow$ absorption.

In particular, for σ^- excitation energy $E \geqslant E_g + \Delta$, the selection rules, governed by conservation of spin angular momentum, permit HH $\uparrow\rightarrow$ CB $\uparrow$ ($\alpha\uparrow$), LH $\uparrow\rightarrow$ CB $\downarrow$ ($\alpha\downarrow$), and SH $\uparrow\rightarrow$ CB $\downarrow$ ($\alpha\downarrow$) transitions. On the other hand for σ^+, HH $\downarrow\rightarrow$ CB $\downarrow$ ($\alpha\downarrow$), LH $\downarrow\rightarrow$ CB $\uparrow$ ($\alpha\uparrow$), and SH $\downarrow\rightarrow$ CB $\uparrow$ ($\alpha\uparrow$) are the allowed transitions. The strengths of the transition for HH and SH are, respectively, 3 and 2 times greater than that for the LH transition [30]. For energies

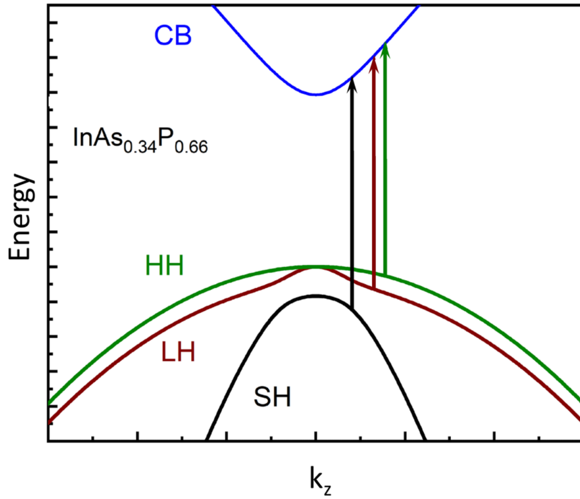

FIG. 8. Sample schematic band structure at $B = 0$ showing the allowed optical transitions between the SH, LH, HH, and CB for a circularly polarized photon of energy greater than $E_g + \Delta$.

$E_g \leqslant E \leqslant E_g + \Delta$, only LH and HH transitions can occur, thereby resulting in the following maximum net spin polarization:

$$S_+ = \frac{1}{2}\left(\frac{\alpha \uparrow - \alpha \downarrow}{\alpha \uparrow + \alpha \downarrow}\right) = \frac{1}{2}\left(\frac{1-3}{1+3}\right) = -\frac{1}{4} \tag{9a}$$

for σ^+ and

$$S_- = \frac{1}{2}\left(\frac{\alpha \uparrow - \alpha \downarrow}{\alpha \uparrow + \alpha \downarrow}\right) = \frac{1}{2}\left(\frac{3-1}{3+1}\right) = \frac{1}{4} \tag{9b}$$

for σ^- polarization. For $E \geqslant E_g + \Delta$ transitions from SH bands are also possible. However, since SH, LH, and HH transitions occur at different nonzero $\mathbf{k}$ and the band masses are different, the joint density of states is different for them. Also, due to nonzero band mixing at $\mathbf{k} \neq 0$, the strength of the transitions is not exactly 3:2:1. All of these contribute to a small, but nonzero, spin polarization [31].

As an example, Fig. 9 shows spin polarization as a function of photon energy for both σ^+ and σ^- helicities. The dashed vertical line shows the spin polarization magnitude of 0.05 at a pump energy of 1.305 eV (950 nm), which is small but not zero. The spin polarization seems to be close to ± 0.25 at around a band gap energy of 0.986 eV.

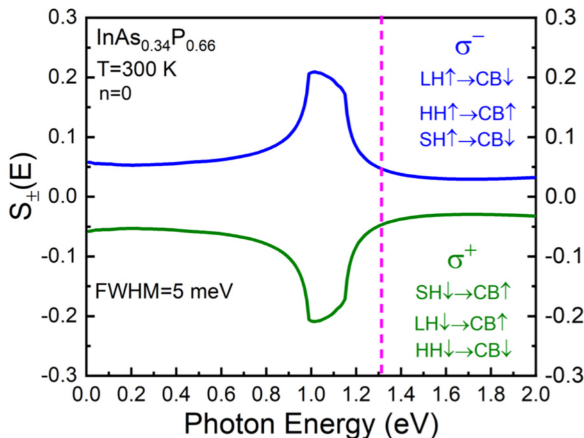

FIG. 9. Sample spin polarization at $B = 0$ for $InAs_{0.34}P_{0.66}$ for σ^+ (green) and σ^- (blue) helicities at $T = 300$ K and zero magnetic field with the broadening FWHM = 5 meV.

A. Spin relaxation

The spin polarizations mentioned above are at the instant of excitation, which decays due to processes like carrier recombination and spin relaxation. Right after the photoexcited spin polarization, the electrons thermalize to become hot electrons through electron-electron scattering among themselves. What then follows is the relaxation of the momentum of the hot electrons by means of momentum scattering with LO phonons, ionized impurity, alloy centers, etc., with a characteristic momentum scattering time τ of a few picoseconds [32]. In this process, the electron spin polarization (magnetization) also dissipates, which is characterized by spin relaxation time τ_s. This can be measured by time-resolved Kerr rotation of an ultrafast probe light of linear polarization since the transient Kerr rotation is directly proportional to the spin polarization [33]. The details of the spin relaxation are provided in Appendix A. The measured spin relaxation times in this study are compared with the calculated ones using Dyanokov-Perel (DP) [34] and Elliot-Yafet (EY) [35,36] mechanisms.

Now we discuss the connection between momentum scattering and spin relaxation. We start with the EY mechanism [35,36], according to which spin dephasing occurs due to spin-orbit interaction. In NGSs with large spin-orbit splitting Δ (such as InAs and InSb) as well as the Rashba effect [37], the conduction bands states are an admixture of both spin-up and spin-down states. Right after an event of momentum scattering due to the lattice or impurities, an electron can scatter to a different spin state than it was in before. This results in the spin dephasing in the EY mechanism. Using the perturbative method, the spin relaxation time τ_s in the nondegenerate limit is given as [38]:

$$\frac{1}{\tau_s^{\mathrm{EY}}} = A\beta^2 \frac{(\alpha k_B T)^2}{E_g} \frac{1}{\tau}, \tag{10a}$$

with

$$\alpha \approx \gamma \left(\frac{1 - \frac{\gamma}{2}}{1 - \frac{\gamma}{3}}\right). \tag{10b}$$

Here τ is the momentum relaxation time, and A is determined by the dominant momentum relaxation process. Here E_g and m_e are the band gap and the electron effective mass, respectively. On the other hand, in semiconductors such as GaAs and InP, Δ is small due to weak spin-orbit coupling. But due to the bulk inversion asymmetry of the crystal structure, spin splitting occurs in the conduction bands such that they become nondegenerate for $\mathbf{k} \neq 0$. This is called the *Dresselhaus* effect [39]. This $\mathbf{k}$-dependent splitting can be thought of as being due to a $\mathbf{k}$-dependent effective magnetic field $\mathbf{B}_{\mathrm{Eff}}(\mathbf{k})$.

The spin polarization components in Eq. (A1) undergo precession around the direction of $\mathbf{B}_{\mathrm{Eff}}(\mathbf{k})$ with a $\mathbf{k}$-dependent precession frequency. During the momentum scattering events, the electron wave vector $\mathbf{k}$ changes to $\mathbf{k}'$, resulting in a new $\mathbf{B}_{\mathrm{Eff}}(\mathbf{k}')$ with a new direction. Consequently, the precession frequency of the spin polarization components changes,

and spin dephasing occurs. This is called DP spin relaxation [34]. Again, using the perturbative method, it is found that the spin relaxation time τ_s^{DP} is inversely proportional to the momentum relaxation time τ in the nondegenerate limit [38] and is given by:

$$\frac{1}{\tau_s^{\mathrm{DP}}} = Q\beta^2 \frac{(k_B T)^3}{\hbar^2 E_g}\tau, \tag{11a}$$

with

$$\beta \approx \frac{4\gamma}{\sqrt{3-\gamma}}\frac{m_e}{m_0}, \tag{11b}$$

where

$$\gamma \approx \frac{\Delta}{E_g + \Delta}. \tag{11c}$$

The momentum relaxation time τ is fundamental to the spin relaxation times, with both DP and EY mechanisms, and it can be related to the dc mobility μ by:

$$\mu = \frac{e\tau}{m_e} \Rightarrow \tau = \frac{\mu m_e}{e}. \tag{12}$$

τ and μ depend on the type of scattering the electrons undergo. In order to calculate the spin relaxation time in the absence of a magnetic field using the DP mechanism in Eq. (11) and the EY mechanism in Eq. (10), we first calculate the dc mobility μ and momentum relaxation time τ for all three different scattering mechanisms mentioned in Appendix B. We recall that the material parameters ϵ_s, ϵ_∞, θ, m_e, and a in $InAs_xP_{1-x}$ are a function of the As concentration x through the linear interpolation [28,32]. For example, the effective mass m_e and ϵ_s are given by:

$$m_e(x) = x m_{e,\mathrm{InAs}} + (1-x) m_{e,\mathrm{InP}} \tag{13a}$$

and

$$\epsilon_s(x) = x\epsilon_{s,\mathrm{InAs}} + (1-x)\epsilon_{s,\mathrm{InP}}. \tag{13b}$$

Figure 10(a) shows the theoretical estimation of μ as a function of the As concentration x for different momentum scattering processes. The green curve corresponds to the mobility μ_{LO} due to the LO scattering given by Ehrenreich's formula in Eq. (B1). The orange curve represents the mobility μ_{Im} due to the impurity scattering using Eq. (B2), and the mobility μ_{Al} is due to the alloy scattering (purple curve) in Eq. (B3). The black curve in Fig. 10 represents the effective mobility μ_{Eff} calculated using Matthiessen's rule:

$$\frac{1}{\mu_{\mathrm{Eff}}} = \frac{1}{\mu_{\mathrm{LO}}} + \frac{1}{\mu_{\mathrm{Im}}} + \frac{1}{\mu_{\mathrm{Al}}}, \tag{14}$$

where it is assumed that these scattering processes are independent of each other. Meanwhile, the dashed blue curve represents the mobility obtained by using the interpolation between the mobilities of InAs and InP [40], given by:

$$\mu_{\mathrm{IP}} = x\mu_{\mathrm{InAs}} + (1-x)\mu_{\mathrm{InP}} - x(1-x)b. \tag{15}$$

Here for electron density $n = 1.0\times10^{17}\,\mathrm{cm}^{-3}$, we use $\mu_{\mathrm{InP}} = 2500\,\mathrm{cm}^2\,\mathrm{V}^{-1}\,\mathrm{s}^{-1}$ using Hilsum's formula [41] and $\mu_{\mathrm{InAs}} = 25\,000\,\mathrm{cm}^2\,\mathrm{V}^{-1}\,\mathrm{s}^{-1}$ [9]. The bowing parameter $b = 30\,000\,\mathrm{cm}^2\,\mathrm{V}^{-1}\,\mathrm{s}^{-1}$ [40].

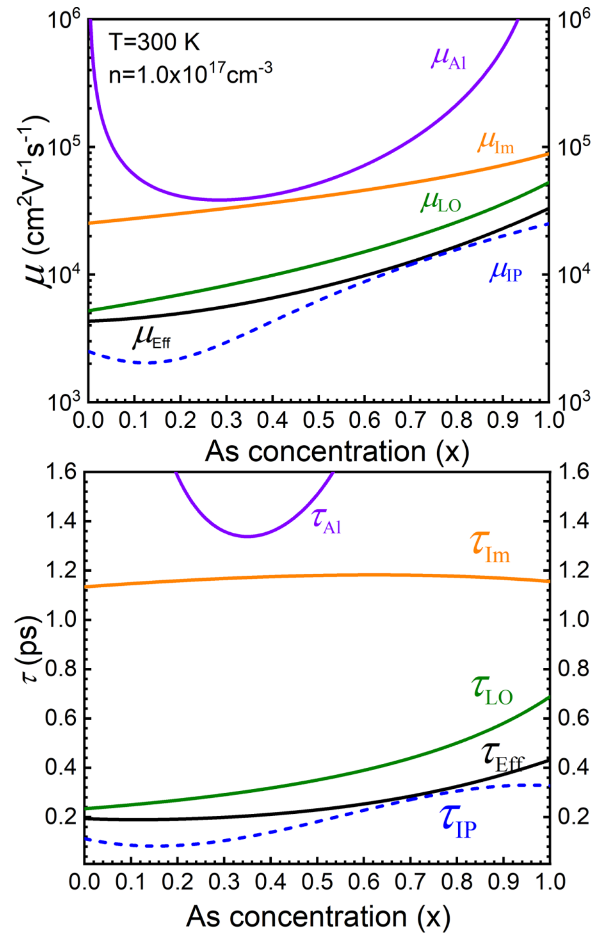

FIG. 10. Top: Calculated dc mobilities for $InAs_xP_{1-x}$ due to LO scattering (green), ionized-impurity scattering (orange), and alloy scattering (purple). The black curve represents effective mobility, and the blue dashed curve shows mobility from direct interpolation. Bottom: Momentum relaxation time using Eq. (12).

The effective mobility (black curve) suggests that LO scattering is the dominant process, followed by ionized-impurity scattering. The alloy scattering is the least significant process. However, between $x = 0.3$ and $x = 0.5$, it is comparable with the ionized-impurity scattering. The direct interpolation method can be a good approximation of the effective mobility due to its very close proximity. The momentum relaxation times vary somewhat differently, as shown in the bottom graph. This may be attributed to the x dependence of the electron effective mass m_e in the mobility formula in Eq. (12). The momentum relaxation time τ was calculated and can be used to obtain the spin relaxation time, under the DP mechanism in Eq. (11) and the EY mechanism in Eq. (10).

Figure 11 shows the spin relaxation under the DP mechanism. The relaxation time $\tau_{\mathrm{Eff}}^{\mathrm{DP}}$ represented by the black curve corresponds to the effective momentum relaxation time τ_{Eff}, whereas $\tau_{\mathrm{IP}}^{\mathrm{DP}}$ corresponds to τ_{IP}. Since LO scattering dominates the momentum relaxation process, we assume $Q = 0.8$ [9,38]. The DP relaxation time for $InAs_{0.34}P_{0.66}$ is around 360 ps, as shown in Fig. 11(b), whereas for pure InAs it is around 40 ps, as shown in Fig. 11(a), which is in good agreement with the calculation by Murzyn *et al.* [9], with $m_e = 0.026m_0$

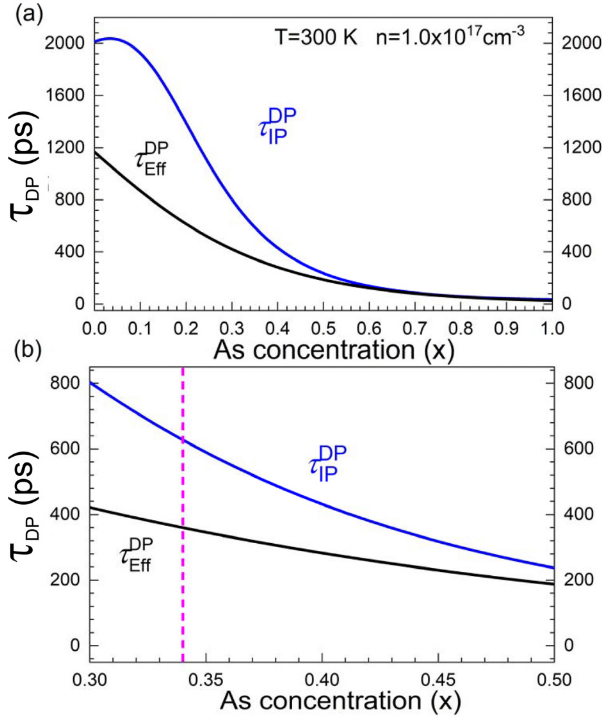

FIG. 11. (a) Calculated DP spin relaxation time as a function of As concentration x for $InAs_xP_{1-x}$. (b) Expanded view, with the vertical dashed line showing the values for $InAs_{0.34}P_{0.66}$.

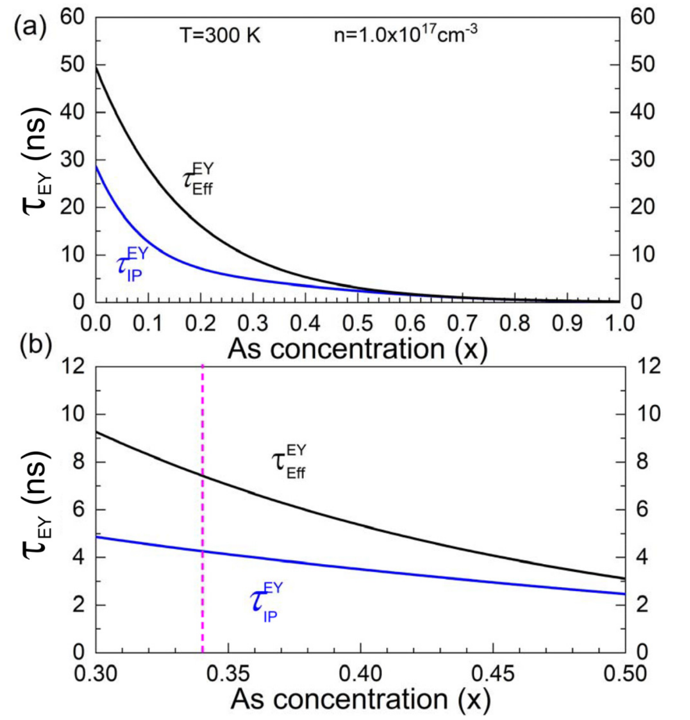

FIG. 12. (a) Calculated EY spin relaxation time as a function of As concentration x for $InAs_xP_{1-x}$. (b) Expanded view, with the vertical dashed line showing the values for $InAs_{0.34}P_{0.66}$.

for InAs, which is slightly different from our estimated $m_e = 0.023m_0$.

On the other hand, Fig. 12 shows the spin relaxation under the EY mechanism. The black curve represents the relaxation time $\tau_{\rm Eff}^{\rm EY}$ corresponding to the effective momentum relaxation time $\tau_{\rm Eff}$, and $\tau_{\rm IP}^{\rm EY}$ corresponds to $\tau_{\rm IP}$. For this calculation, we set $A = 2.0$ in Eq. (10) due to dominating LO scattering [38]. The EY relaxation time for $InAs_{0.34}P_{0.66}$ is around 6 ns, as shown in Fig. 12(b).

A closer look at Fig. 12(a) shows that for pure InAs, the relaxation time is around 184 ps. Like in the DP case, very good agreement between the effective and interpolated relaxation times are obtained for x larger than 0.5. In Table II, we present a comparison between the experimental and calculated values of the spin relaxation times for $InAs_{0.34}P_{0.66}$. The last column contains the relaxation times obtained from the TRKR data in Fig. 7; here τ_1 and τ_2 are taken from the biexponential fit in Fig. 7(a), while τ_3 and τ_4 are taken from the exponential fit in Fig. 7(b). Although they are taken from somewhat different data sets, τ_2 and τ_3 can be considered to equally represent the same relaxation process.

Since the excitation energy of 1.305 eV is more than $E_g + \Delta = 1.154$ eV, the photoexcited electrons are hot [42], and it may be that $\tau_1 = 7.24$, $\tau_2 = 38.2$, and $\tau_3 = 39.1$ ps correspond to the loss of spin polarization due to the thermalization of these hot electrons by electron-electron scattering and electron-phonon scattering [43]. At the same time, the electrons may also lose their original spin orientation due to trapping in the impurity centers [44]. Due to strong spin-orbit interaction between the hole bands, the relaxation of hole spins also occurs around the same time. It can therefore be concluded that the longer relaxation time $\tau_4 = 394$ ps corresponds to the electrons' spin polarization.

The calculated DP relaxation times $\tau_{\rm Eff}^{\rm DP} = 359$ ps and $\tau_{\rm IP}^{\rm DP} = 626$ ps are based on the effective momentum scattering times $\tau_{\rm Eff}$ and the interpolated scattering time $\tau_{\rm IP}$, respectively. The electron effective masses are also taken from the linear interpolation. Our experimental value of $\tau_4 = 394$ ps shows very good agreement with the calculated DP relaxation time $\tau_{\rm Eff}^{\rm DP}$. However, the EY relaxation times overestimate τ_4 by at least an order of magnitude, which could be because the

TABLE II. Comparison of the calculated spin relaxation times with the experimental fits for $InAs_{0.34}P_{0.66}$.

μ (cm^2 V^{-1} s^{-1})	τ (ps)	$\tau_{\rm DP}$ (ps)	$\tau_{\rm EY}$ (ps)	τ_s (ps), Expt.
$\mu_{\rm Eff} = 5956$	$\tau_{\rm Eff} = 0.203$	$\tau_{\rm Eff}^{\rm DP} = 359$	$\tau_{\rm Eff}^{\rm EY} = 7420$	$\tau_1 = 7.24 \pm 1.15$
				$\tau_2 = 38.2 \pm 1.66$
$\mu_{\rm IP} = 3418$	$\tau_{\rm IP} = 0.117$	$\tau_{\rm IP}^{\rm DP} = 626$	$\tau_{\rm IP}^{\rm EY} = 4260$	$\tau_3 = 39.1 \pm 1.38$
				$\tau_4 = 394 \pm 39.6$

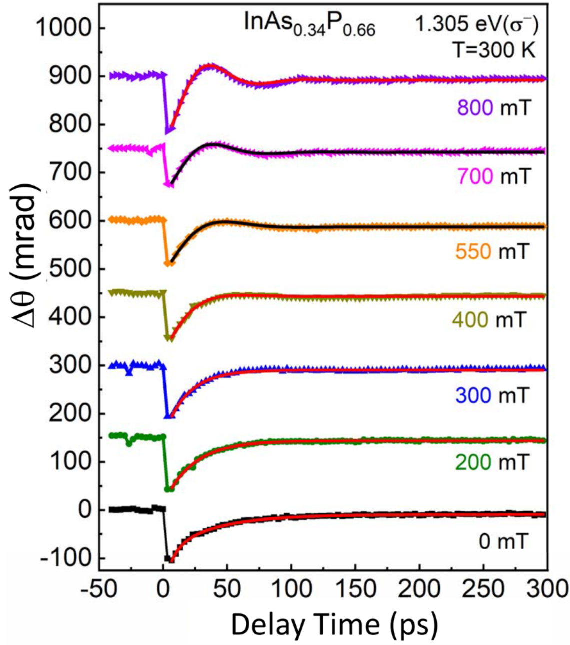

FIG. 13. Magneto-optical kerr effect (MOKE) at different magnetic fields. Solid lines without symbols represent fitting with a damping function.

spin-orbit interaction in $InAs_{0.34}P_{0.66}$ is not as strong as those of InAs and InSb [9,45,46].

Also, the estimated mobility from the linewidth of the CR measurement is around 810 $cm^2\,V^{-1}\,s^{-1}$, which suggests a low momentum scattering time τ. However, we note that this estimation could be premature because the CR resonance occurs at a very high magnetic field (around 75 T), and an accurate magnetic dependence of the mobility is unavailable at this time. Nonetheless, since the DP relaxation time is related inversely to τ, this supports the argument for the DP mechanism being the dominant relaxation mechanism for the spin.

An earlier study on n-type GaAs samples with low mobilities showed very long spin lifetimes [29] under the DP mechanism. However, in another study of high-mobility GaAs, the DP mechanism was suppressed [47] as well as in n-type InAs [9]. In a related study of an undoped $InAs_{0.4}P_{0.6}$ film, the spin relaxation time showed a sensitive response to excitation energies and temperature [16]. Therefore, it is clear that the spin relaxation time in III-V semiconductors depends on many factors such as mobility, doping density, temperature, photoexcitation energy, and intensity. For a more definitive conclusion, further explorations including several of these factors are necessary.

B. Effect of magnetic field on spin polarization

As an important extension, we also study the effect of weak magnetic fields at RT on the spin relaxation in the Voigt configuration under the same experimental conditions as in the previous section. As shown in Appendix B, the presence of such a field results in a precession of the spin polarization about the field, with Larmor's frequency given as:

$$\Omega = \frac{g\mu_B B}{\hbar}. \tag{16}$$

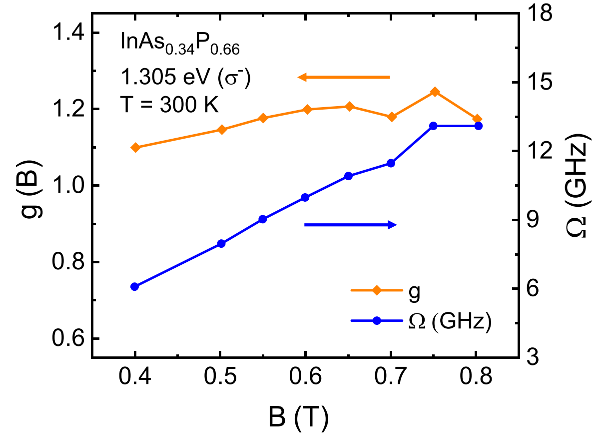

FIG. 14. Magnetic field dependence of Larmor's frequency (blue) and the effective g-factor (orange) for $InAs_{0.34}P_{0.66}$.

Figure 13 shows TRKR for $InAs_{0.34}P_{0.66}$ at different magnetic fields B, including 0 and 800 mT, where the colored symbols represent the experimental data. The solid lines without symbols are from fitting the data beyond the delay time of 0 ps. The data at 0, 200, and 300 mT are fitted with $\Delta\theta \approx e^{-\frac{t}{\tau}}$ due to the absence of oscillation. On the other hand, the data at 400, 550, 700, and 800 mT are fitted with an oscillating decay function, $\Delta\theta \approx e^{-\frac{t}{\tau}} \sin(\Omega t + \phi_0)$, where τ is the spin relaxation time and Ω is Larmor's frequency. In Figs. 14(a) and 14(b), we show the B dependence of Larmor's frequency Ω and the effective g-factor calculated based on Eq. (16).

The g-factor as determined by the experimental TRKR is different from the calculation done in the previous sections based on the simple Kane-like model, for which we found the g-factor was close to zero. This is not surprising, and as pointed out by Pfeffer and Zawadzki [48], the expression for the band edge g-factor, g_0^* given in Eq. (4), is valid for NGSs but needs to be modified for medium-gap semiconductors to take into account higher bands. As a result, the simple model predicts a g-factor close to zero, but in fact, the TRKR measurements show that it is most likely closer to -1 (we note that the TRKR measurements do not give the sign of the g-factor). This indicates that the alloy concentration x for a zero g-factor is most likely less than 0.34. We note, however, that the simple Kane-like model is sufficient to determine the cyclotron's effective masses.

V. CONCLUSIONS

In this work, we experimentally studied the magneto-optical properties of $InAs_xP_{1-x}$ films at RT by employing ultrahigh magnetic fields (by employing CR measurements) and compared our results, with good agreement, with two different theoretical models. The InAsP alloys have important applications for devices owing to the possibility of changing the gap from 0.36 to 1.35 eV, which covers a broad optical spectrum from mid- to near infrared, as well as the possibility of designing a material with the right alloy concentration x that has a g-factor close to zero.

Theoretical calculations were based on the Pidgeon-Brown model as well as a simpler, single-band, nonparabolic model

that we previously used to investigate effective masses in near-surface InAs quantum wells [12]. To describe our CR experiments, we used a simpler, single, nonparabolic model since this avoids the need to determine how the many parameters in the Pidgeon-Brown model vary with alloy concentration. We found that our simpler model produced excellent agreement with the experimental results for the CR masses and their dependence on alloying using just a simple linear interpolation of both the band gap and spin-orbit splitting. The simple model also predicted a g-factor close to zero for the concentration $x = 0.34$.

Furthermore, for our reported time-resolved measurements, we needed to use the full Pidgeon-Brown model since both the conduction band and valence band Landau levels are needed to determine the spin polarization relaxation. Using the FWHM of the experimental CR curves, the AC electron mobilities can be estimated. This information was used to model the time resolved magneto-optical kerr effect (TRMOKE) and to estimate the spin relaxation time in a low magnetic field regime in the Voigt configuration.

The observed precession of the spin polarization with the B-dependent Larmor's frequency (at low magnetic fields) was also used to estimate the effective g-factor for $InAs_{0.34}P_{0.66}$. These results showed that the g-factor is not zero for $x = 0.34$, but probably closer to -1. This indicates that while the simple model does very well in predicting the CR effective masses at high magnetic fields, it does not do as well for the g-factor. This is not surprising since $InAs_xP_{1-x}$ for $x = 0.34$ is a medium-gap material. While the simple model presented here for modeling the g-factor works well for NGSs, it has been pointed out in the literature that for medium-gap materials, coupling to higher conduction bands can influence the value of the g-factor [6,48].

A thorough analysis of the g-factor suggests the potential for engineering a zero-g-factor InAsP alloy. Our results showed that the proper As concentration for a zero g-factor most likely is slightly less than the current value of $x = 0.34$ predicted by the simple model presented in this study.

ACKNOWLEDGMENTS

This material is based upon work supported by the Air Force Office of Scientific Research under Awards No. FA9550-14-1-0376 and No. FA9550-17-1-0341 and DURIP funding (Award No. FA9550-16-1-0358). G.A.K. and B.A.M. acknowledge the support from the Japanese visiting program of the Institute for Solid State Physics, University of Tokyo. G.A.K. also acknowledges the support from an L. C. Hassinger Fellowship.

APPENDIX A: BLOCH EQUATIONS FOR SPIN RELAXATION

The dissipation of the spin polarization can be described by Bloch equations for a homogeneous spin polarization vector function $\mathbf{S(t)}$ in a magnetic field, say, $\mathbf{B} = (0, 0, B_0)$, as:

$$\frac{dS_x}{dt} = -\Omega S_y + \frac{S_x}{T_2} \tag{A1a}$$

and

$$\frac{dS_y}{dt} = -\Omega S_x + \frac{S_y}{T_2} \tag{A1b}$$

for the transverse components. Here Ω is Larmor's frequency, with which the S_x and S_y precess around B_z, given by

$$\Omega = \frac{g\mu_B B_z}{\hbar}, \tag{A1c}$$

where g is the electron g-factor and μ_B is Bohr's magneton. For the longitudinal component we have

$$\frac{dS_z}{dt} = \frac{S_0 - S_z}{T_1}, \tag{A1d}$$

where S_0 is the equilibrium spin polarization due to B_0. T_1 is called the longitudinal relaxation time, which is the time taken by S_z to reach its equilibrium value S_0. It involves loss of energy from the spin system due to scattering with the lattice and therefore is equivalent to the thermalization time of the spin system with the lattice [30]. T_2 is called the spin dephasing time, during which the phases of the transverse components S_x and S_y are destroyed due to the spatiotemporal fluctuations in the precession frequency Ω brought about due to momentum scattering. In cubic isotropic semiconductors, T_1 and T_2 can be approximated to be equal when $\mathbf{B}$ is not very high [30]. Hereafter, we call T_1 and T_2 the spin relaxation time τ_s.

APPENDIX B: ESTIMATION OF THE MOBILITIES

The mobility μ_{LO} due to LO scattering given by Ehrenreich's variational calculation is [49,50]:

$$\mu_{LO} = \frac{4e\hbar}{3\sqrt{\pi m_e^3 R k_B T}}\left(\frac{\epsilon_s\epsilon_\infty}{\epsilon_s - \epsilon_\infty}\right)\left(\frac{e^{\theta/T} - 1}{\theta/T}\right)G^{(1)}e^{-\xi}. \tag{B1}$$

Here ϵ_s and ϵ_∞ are the low- and high-frequency dielectric constants, respectively. θ is the optical phonon Debye temperature, and $R = 13.6$ eV is Rydberg's constant. $G^{(1)}e^{-\xi}$ is estimated from the calculation in Ref. [49]. Electrons lose momentum by scattering with the impurities as well. According to Brooks [51,52], the electron mobility due to ionized impurity scattering is given by:

$$\mu_{Im} = \frac{128\sqrt{2\pi}}{N_I e^3\sqrt{m_e}}(\epsilon_s\epsilon_0)^2(k_B T)^{3/2}\left(ln\left(1 + \gamma_B^2\right) - \frac{\gamma_B^2}{1 + \gamma_B^2}\right)^{-1}, \tag{B2a}$$

with

$$\gamma_B^2 = 24\frac{m_e(\epsilon_s\epsilon_0)(k_B T)^2}{e^2\hbar^2 N_I}. \tag{B2b}$$

Here ϵ_0 is the permittivity of free space, and N_I is the density of impurity and is approximated by a constant density of 1.0×10^{17} cm^{-3}.

Since $InAs_xP_{1-x}$ is a semiconductor alloy, it is important to consider the mobility due to alloy scattering. It is given by [32,53,54]:

$$\mu_{Al} = \frac{128\sqrt{2}e\hbar^4}{9\pi^{3/2}(\Delta E_{Al})^2(k_B T)^{1/2}}\frac{1}{m_e^{1/5}x(1 - x)a^3}, \tag{B3}$$

where x is the alloy ratio, a is the lattice constant of the alloy, and ΔE_{Al} is the alloy scattering potential, which is set equal to 0.581 [32]. The material parameters involved in the above equations, including ϵ_s, ϵ_∞, θ, m_e, and a, are obtained by using linear interpolation between InAs and InP [28,32]. Therefore, they are also functions of the As concentration x.

However, since the prefactors Q and A involved in Eqs. (11) and (10) vary for different momentum scattering processes, it is suggested that the best way is to measure the mobility of the sample using different experimental methods such as the Hall effect. In our case, alternatively, the estimated mobilities in Sec. II from the CR measurements can be the starting point for estimating the momentum relaxation time using Eq. (12).

[1] M. Wada and H. Hosomatsu, Wide wavelength and low dark current lattice-mismatched InGaAs/InAsP photodiodes grown by metalorganic vapor-phase epitaxy, Appl. Phys. Lett. **64**, 1265 (1994).

[2] H. Sugiura, MOMBE growth of InAsP laser materials, J. Cryst. Growth **164**, 434 (1996).

[3] D. Elvira, R. Hostein, B. Fain, L. Monniello, A. Michon, G. Beaudoin, R. Braive, I. Robert-Philip, I. Abram, I. Sagnes, and A. Beveratos, Single $InAs_{1-x}P_x$/InP quantum dots as telecommunications-band photon sources, Phys. Rev. B **84**, 195302 (2011).

[4] A. Bernard, M. Ravaro, I. Roland, J.-M. Gérard, M. Krakowski, O. Parillaud, B. Gérard, I. Favero, and G. Leo, Mid-infrared optical characterization of InGaAsP, J. Opt. Soc. Am. B **35**, C25 (2018).

[5] R. Vrijen and E. Yablonovitch, A spin-coherent semiconductor photo-detector for quantum communication, Phys. E (Amsterdam, Neth.) **10**, 569 (2001).

[6] R. J. Nicholas, R. A. Stradling, and J. C. Ramage, Evidence for a reduction in the momentum matrix element P^2 due to alloy disorder in $InAs_{1-x}P_x$, J. Phys. C **12**, 1641 (1979).

[7] H. Ehrenreich, Electron mobility of indium arsenide phosphide $[In(As_yP_{1-y})]$, J. Phys. Chem. Solids **12**, 97 (1959).

[8] S. G. Choi, C. J. Palmstrøm, Y. D. Kim, D. E. Aspnes, H. J. Kim, and Y.-C. Chang, Dielectric functions and electronic structure of $InAs_xP_{1-x}$ films on InP, Appl. Phys. Lett. **91**, 041917 (2007).

[9] P. Murzyn, C. R. Pidgeon, P. J. Phillips, M. Merrick, K. L. Litvinenko, J. Allam, B. N. Murdin, T. Ashley, J. H. Jefferson, A. Miller, and L. F. Cohen, Suppression of D'yakonov-Perel spin relaxation in InAs and InSb by n-type doping at 300 K, Appl. Phys. Lett. **83**, 5220 (2003).

[10] K. C. Hall, W. H. Lau, K. Gündoğdu, M. E. Flatté, and T. F. Boggess, Nonmagnetic semiconductor spin transistor, Appl. Phys. Lett. **83**, 2937 (2003).

[11] R. N. Kini, K. Nontapot, G. A. Khodaparast, R. E. Welser, and L. J. Guido, Time resolved measurements of spin and carrier dynamics in InAs films, J. Appl. Phys. **103**, 064318 (2008).

[12] J. Yuan, M. Hatefipour, B. A. Magill, W. Mayer, M. C. Dartiailh, K. Sardashti, K. S. Wickramasinghe, G. A. Khodaparast, Y. H. Matsuda, Y. Kohama, Z. Yang, S. Thapa, C. J. Stanton, and J. Shabani, Experimental measurements of effective mass in near-surface InAs quantum wells, Phys. Rev. B **101**, 205310 (2020).

[13] H. Ma, Z. Jin, L. Wang, and G. Ma, Electron spin relaxation in intrinsic bulk InP semiconductor, J. Appl. Phys. **109**, 023105 (2011).

[14] B. Li, M. C. Tamargo, and C. A. Meriles, Electron spin dynamics in Fe-doped InP, Appl. Phys. Lett. **91**, 222114 (2007).

[15] M. Ikezawa, B. Pal, Y. Masumoto, I. V. Ignatiev, S. Yu. Verbin, and I. Ya. Gerlovin, Submillisecond electron spin relaxation in InP quantum dots, Phys. Rev. B **72**, 153302 (2005).

[16] M. A. Meeker, B. A. Magill, T. R. Merritt, M. Bhowmick, K. McCutcheon, G. A. Khodaparast, J. G. Tischler, S. McGill, S. G. Choi, and C. J. Palmstrøm, Dynamics of photoexcited carriers and spins in InAsP ternary alloys, Appl. Phys. Lett. **102**, 222102 (2013).

[17] T. R. Merritt, M. A. Meekerand, Brenden A Magill, G. A. Khodaparast, S. McGill, J. G. Tischler, S. G. Choi, and C. J. Palmstrøm, Spin relaxation of conduction electrons in bulk III-V semiconductors, J. Appl. Phys. **115**, 193503 (2014).

[18] G. D. Sanders, Y. Sun, F. V. Kyrychenko, C. J. Stanton, G. A. Khodaparast, M. A. Zudov, J. Kono, Y. H. Matsuda, N. Miura, and H. Munekata, Electronic states and cyclotron resonance in n-type InMnAs, Phys. Rev. B **68**, 165205 (2003).

[19] G. A. Khodaparast, Y. H. Matsuda, D. Saha, G. D. Sanders, C. J. Stanton, H. Saito, S. Takeyama, T. R. Merritt, C. Feeser, B. W. Wessels, X. Liu, and J. Furdyna, Cyclotron resonance in ferromagnetic InMnAs and InMnSb, Phys. Rev. B **88**, 235204 (2013).

[20] Y. Sun, F. V. Kyrychenko, G. D. Sanders, C. J. Stanton, G. A. Khodaparast, J. Kono, Y. H. Matsuda, and H. Munekata, Probe of the band structure of MBE grown p-type InMnAs at ultrahigh magnetic fields, SPIN **5**, 1550002 (2015).

[21] C. R. Pidgeon and R. N. Brown, Interband Magneto-absorption and Faraday Rotation in InSb, Phys. Rev. **146**, 575 (1966).

[22] J. G. Mavroides, Magneto-optical properties, in *Optical Properties of Solids*, edited by F. Abelès (North-Holland, Amsterdam, 1972), pp. 351–528.

[23] R. Bowers and Y. Yafet, Magnetic susceptibility of InSb, Phys. Rev. **115**, 1165 (1959).

[24] B. Lax and J. G. Mavroides, Cyclotron resonance, Solid State Phys. **XI**, 261 (1960).

[25] Y.-G. Zhao, R. A. Masut, J. L. Brebner, C. A. Tran, and J. T. Graham, Temperature dependence of photoluminescence in InAsP/InP strained multiple quantum wells, J. Appl. Phys. **76**, 5921 (1994).

[26] H. Kosaka, A. A. Kiselev, F. A. Baron, K. W. Kim, and E. Yablonovitch, Electron g factor engineering in III-V semiconductors for quantum communications, Electron. Lett. **37**, 464 (2001).

[27] G. A. Khodaparast, R. C. Meyer, X. H. Zhang, T. Kasturiarachchi, R. E. Doezema, S. J. Chung, N. Goel, M. B. Santos, and Y. J. Wang, Time resolved measurements of spin and carrier dynamics in InAs films, Phys. E (Amsterdam, Neth.) **20**, 386 (2004).

[28] I. Vurgaftman, J. R. Meyer, and L. R. Ram-Mohan, Band parameters for III-V compound semiconductors and their alloys, J. Appl. Phys. **89**, 5815 (2001).

[29] J. M. Kikkawa and D. D. Awschalom, Resonant Spin Amplification in *n*-Type GaAs, Phys. Rev. Lett. **80**, 4313 (1998).

[30] I. Žutić, J. Fabian, and S. Das Sarma, Spintronics: Fundamentals and applications, Rev. Mod. Phys. **76**, 323 (2004).

[31] A. V. Kimel, A. A. Tsvetkov, A. Kirilyuk, Th. Rasing, and V. N. Gridnev, Picosecond dynamics of bleaching and spin splitting in InP revealed by the photoinduced magneto-optical Kerr effect near the spin-orbit split-off exciton transition, Phys. Rev. B **69**, 165214 (2004).

[32] M. K. Hudait, Y. Lin, P. M. Sinha, J. R. Lindemuth, and S. A. Ringel, Carrier compensation and scattering mechanisms in Si-doped $InAs_yP_{1-y}$ layers grown on InP substrates using intermediate $InAs_yP_{1-y}$ step-graded buffers, J. Appl. Phys. **100**, 063705 (2006).

[33] Y. Sun, Theoretical studies of the electronic, magneto-optical and transport properties of diluted magnetic semiconductors, Ph.D. thesis, University of Florida, 2005.

[34] M. I. Dyakonov and V. I. Perel, Theory of optical spin orientation of electrons and nuclei in semiconductors, in *Modern Problems in Condensed Matter Sciences: Optical Orientation*, edited by F. Meier and B. P. Zakharchenya (Elsevier, Amsterdam, 1984), Chap. 2, Vol. 8, pp. 11–13, 15–71.

[35] R. J. Elliott, Theory of the effect of spin-orbit coupling on magnetic resonance in some semiconductors, Phys. Rev. **96**, 266 (1954).

[36] Y. Yafet, *g*-Factors and spin-lattice relaxation of conduction electrons, Solid State Phys. **14**, 1 (1963).

[37] G. A. Khodaparast, R. E. Doezema, S. J. Chung, K. J. Goldammer, and M. B. Santos, Spectroscopy of Rashba spin splitting in InSb quantum wells, Phys. Rev. B **70**, 155322 (2004).

[38] B. N. Murdin, K. Litvinenko, J. Allam, C. R. Pidgeon, M. Bird, K. Morrison, T. Zhang, S. K. Clowes, W. R. Branford, J. Harris, and L. F. Cohen, Temperature and doping dependence of spin relaxation in *n*-InAs, Phys. Rev. B **72**, 085346 (2005).

[39] G. Dresselhaus, Spin-orbit coupling effects in zinc blende structures, Phys. Rev. **100**, 580 (1955).

[40] S. Adachi, *Carrier Transport Properties, in Properties of Semiconductor Alloys* (John Wiley & Sons, Hoboken, NJ, 2009), Chap. 12.

[41] New semiconductor materials. Characteristics and properties, http://www.ioffe.ru/SVA/.

[42] J. Shah, *Ultrafast Spectroscopy of Semiconductors and Semiconductor Nanostructures* (Springer, Berlin, Heidelberg, 1999).

[43] *Optical Orientation*, edited by F. Meier and B. P. Zakharchenya (North-Holland, Amsterdam, 1984).

[44] Y. Mitsumori, A. Oiwa, T. Słupinski, H. Maruki, Y. Kashimura, F. Minami, and H. Munekata, Dynamics of photoinduced magnetization rotation in ferromagnetic semiconductor *p*-(Ga,Mn)As, Phys. Rev. B **69**, 033203 (2004).

[45] M. Frazier, J. G. Cates, J. A. Waugh, J. J. Heremans, M. B. Santos, X. Liu, and G. A. Khodaparast, Photoinduced spin-polarized current in InSb-based structures, J. Appl. Phys. **106**, 103513 (2009).

[46] M. Bhowmick, G. A. Khodaparast, T. D. Mishima, M. B. Santos, D. Saha, G. Sanders, and C. J. Stanton, Interband and intraband relaxation dynamics in InSb based quantum wells, J. Appl. Phys. **120**, 235702 (2016).

[47] R. I. Dzhioev, K. V. Kavokin, V. L. Korenev, M. V. Lazarev, N. K. Poletaev, B. P. Zakharchenya, E. A. Stinaff, D. Gammon, A. S. Bracker, and M. E. Ware, Suppression of Dyakonov-Perel Spin Relaxation in High-Mobility *n*-GaAs, Phys. Rev. Lett. **93**, 216402 (2004).

[48] P. Pfeffer and W. Zawadzki, Temperature dependence of the electron spin g factor in CdTe and InP, J. Appl. Phys. **111**, 083705 (2012).

[49] H. Ehrenreich, Screening effects in polar semiconductors, J. Phys. Chem. Solids **8**, 130 (1959).

[50] P. H. Song and K. W. Kim, Spin relaxation of conduction electrons in bulk III-V semiconductors, Phys. Rev. B **66**, 035207 (2002).

[51] H. Brooks, Theory of the electrical properties of germanium and silicon, Adv. Electron Elect. Phys. **7**, 85 (1955).

[52] C. M. Wolfe, G. E. Stillman, and W. T. Lindley, Electron mobility in high-purity GaAs, J. Appl. Phys. **41**, 3088 (1970).

[53] J. W. Harrison and J. R. Hauser, Theoretical calculations of electron mobility in ternary III-V compounds, J. Appl. Phys. **47**, 292 (1976).

[54] J. J. Tietjen and L. R. Weisberg, Electron mobility in $GaAs_{1-x}P_x$ alloys, Appl. Phys. Lett. **7**, 261 (1965).